Superresolution ultrasound imaging using back-projected reconstruction

G. T. Clement
Department of Radiology, Harvard Medical School, Brigham and Women's Hospital, Boston, Massachusetts 02115

J. Huttunen
University of Kuopio, P. O. Box 1627, Neulaniementie 2, FIN-70211, Finland

K. Hynynen
Department of Radiology, Harvard Medical School, Brigham and Women's Hospital, Boston, Massachusetts 02115

An ultrasound technique for imaging objects significantly smaller than the source wavelength is investigated. Signals from a focused beam are recorded over an image plane in the acoustic farfield and backprojected in the wave-vector domain to the focal plane. A superresolution image recovery method is then used to analyze the Fourier spatial frequency spectrum of the signal in an attempt to deduce the location and size of objects in this plane. The physical foundation for the method is rooted in the fact that high spatial frequencies introduced by the object in fact affect the lower (nonevanescent) spatial frequencies of the overall signal. The technique achieves this by using *a priori* measurements of the ultrasound focus in water, which gives full spectral information about the image source. A guess is then made regarding the size and location of the object that distorted the field, and this is convolved with the *a priori* measurement, thus creating a candidate image. A large number of candidates are generated and the one whose spectrum best matches the uncorrected image is accepted. The method is demonstrated using 0.34- and 0.60-mm wires with a focused 1.05-MHz ultrasound signal and then a human hair ($\sim$0.03 mm) with a 4.7-MHz signal. © 2005 Acoustical Society of America. [DOI: 10.1121/1.2109167]

I. INTRODUCTION

Over the past decade, submillimeter imaging *in vivo* has been the goal of numerous imaging modalities. In medicine this is motivated by the considerable number of potential uses in diagnostics and in the study of biological models. Some of these uses include, but are not limited to, sensing tissue morphological changes, monitoring of disease progression, temperature monitoring, following mouse and chicken embryonic development for genomics and other areas, and monitoring of the vascular system. High-resolution optics, nuclear magnetic resonance (NMR), x-ray computed tomography (CT), and ultrasound have all been examined as methods for performing high-resolution imaging, each with their own unique advantages and disadvantages. Optical coherence tomography (OCT)[1] has been used to perform *in vivo* imaging of tissue interiors in a manner analogous to B-scan ultrasound by using infrared or near infrared light interferometry. Resolution of less than 1 μ has been achieved, but with a penetration depth of only a few millimeters. Magnetic resonance microscopy (μMRI)[2] and CT microscopy have both demonstrated significant progress in high-resolution imaging with deep penetration. However, the cost and large apparatus involved with these methods make them impractical for laboratory or small clinical use.

In ultrasound, high-resolution approaches[3,4] referred to as ultrasound microimaging (UMI) or ultrasound biomicroscopy (UBM) have been applied. Such methods use high-frequency backscattered ultrasound (50–200 MHz) to achieve resolution as low as 20 μ for imaging superficial tissues such as the skin and blood vessels. These techniques have been used for their ability to measure a number of tissue properties that are not readily obtainable with other imaging methods. These properties consist of ultrasound sound speed, attenuation, impedance, tissue stiffness, and temperature sensitivity.

On a practical level ultrasound has been considered an attractive alternative to other methods due to its potential for producing a compact, nonionizing, and very low cost imaging device that could be utilized in a clinical or laboratory setting. The traditional approach applied in both UMI and UBM has been to image at higher ultrasound frequencies. Using these methods, image resolution has been extended to about 10 μ, but with the tradeoff of significantly increased attenuation.

We propose, however, a method that could allow *in vivo* imaging at submillimeter resolution with frequencies up to one order of magnitude lower than previously reported methods. Lower frequencies would allow high-resolution imaging with significantly greater penetration depth. To achieve this, we introduce a new approach to high-resolution ultrasound, which employs a combination of phase-contrast imaging, angular spectral decomposition, and a superresolution reconstruction technique. With this approach, we examine the pos-

sibility of imaging objects located entirely within an ultrasound focus, over a field of view equal to the focal area. In contrast, traditional time-of-flight (TOF) ultrasound resolution is determined by the size of the focal region achieved within the tissue. Our approach could potentially have immediate application in detecting acoustic properties that are not visible optically. In particular, the method would be sensitive to dynamic changes that induce a change in sound speed and could have application in complementing the wide range of biological areas where very-high-frequency ultrasound is being investigated.[5–7]

Superresolution is a general term that describes a wide body of methods that seek to restore an image with spatial resolution greater than the classical diffraction limit.[8] Well-founded methods for imaging objects smaller than the imaging wavelength have been carried out in one of three ways: near-field imaging[9,10] records information within a distance of several wavelengths from the source, in order to collect information from evanescent wave components of the signal, whose magnitude decays exponentially with distance from an object. Time reversal[11] uses information from scattering centers in a highly inhomogeneous field to focus beyond that obtainable in a homogeneous medium.[12] Finally, spectral methods seek to reconstruct higher spatial frequencies beyond the cutoff frequency, using *a priori* information about the image.[8]

Image processing has benefitted significantly from the application of superresolution reconstruction techniques—both near field and, more recently, far field—to a variety of optical[13–20] and electromagnetic imaging applications ranging from array and astronomical data[21] to microscopic systems.[22] The concept and limits of the spectral far-field techniques (which will be exploited in this study) have been examined[17,23] and a superresolution algorithm developed for astronomical imagery at the University of California—San Diego has resulted in the founding of a private company (Pixon, Setauket, NY) dedicated to superresolution image enhancement. A significant amount of earlier work was performed in the areas of holographic superresolution by Sato,[24] including studies in ultrasound. However, this work was limited to reconstruction through correspondence techniques[25] or as an image-processing technique. Superresolution imaging has additionally been applied toward the reconstruction of ultrasonic impedance profiles.[26]

In contrast, we use the term superresolution exclusively in this paper to indicate the recovery of spatial frequencies above the bandwidth that would be propagated by a *single* source beam to an image plane. This reconstruction is restricted to cases of far-field imaging and does not rely on measurement of evanescent waves. The physical foundation for this definition of superresolution is rooted in the fact that propagated spatial information at spatial frequencies below the diffraction limit is not independent of the information above the frequency cutoff. Basic arguments, outlined in the next section, demonstrate that such reconstruction is possible, given certain *a priori* information about the localization of the object or—as we will demonstrate—the nature of the image source.

II. THEORETICAL FOUNDATION

The present problem considers a harmonic, localized, ultrasonic wave $p(\vec{r},t)$ that satisfies the linearized Stokes equation,[27]

$$\left(1 + \tau \frac{\partial}{\partial t}\right)\nabla^2 p(\vec{r},t) = \frac{1}{c^2}\ddot{p}(\vec{r},t), \tag{1}$$

where c is the real sound speed and τ is the relaxation time for the medium. Both of these quantities are, in general, functions of frequency. The projection is considered in Cartesian coordinates, in order to relate the field between two planes at z_i and z_o, referred to as the image planes and the object planes, respectively. A Helmholtz equation

$$\left(\frac{\partial^2}{\partial z^2} + \widetilde{k}^2\right)\widetilde{p}(k_x,k_y,z,\omega) = 0 \tag{2}$$

is obtained by the substitution of a Fourier integral with respect to the x and y coordinates into Eq. (1) where the Cartesian wave numbers are given by k_x and k_y and ω is the angular frequency.[28] To propagate the field from the image plane at z_i to the image plane z_o, the advanced solution of Eq. (2) is used:[29]

$$\widetilde{p}(k_x,k_y,z_o)$$
$$= \widetilde{p}(k_x,k_y,z_i)\exp\left(i(z_o - z_i)\sqrt{\frac{\omega^2}{c^2}\frac{1}{1 + i\tau\omega} - k_x^2 - k_y^2}\right). \tag{3}$$

The exponential term in Eq. (3) serves as a transfer function for the case of a wave travelling in nondissipative homogeneous media. The use of this function for both transmission and backscattered data is well established.[30] However, this function may be readily modified to cover a wide range of situations including, for example, layered media,[31] dispersion,[31] and shear modes,[32] given sufficient information about the media. The generalized form of Eq. (3) for a given frequency is simply

$$\widetilde{p}(k_x,k_y,z_i) = \widetilde{p}(k_x,k_y,z_o)h(k_x,k_y,z_i - z_o), \tag{4}$$

where h is a generalized transfer function relating the object and image planes, which by the convolution theorem requires that

$$p(x,y,z_i) = p(x,y,z_o)\otimes_{x,y}h(x,y,z_i - z_o), \tag{5}$$

representing a two-dimensional convolution with respect to x and y. The insertion of an object $f(x,y,z_o)$ contained entirely within the beam is now considered, so that the field becomes $p(x,y,z_o)f(x,y,z_o)$ immediately after propagating through the object and the field at the image plane in the wave-vector domain becomes

$$\widetilde{p}(k_x,k_y,z_i)$$
$$= [\widetilde{p}(k_x,k_y,z_o)\otimes_{x,y}\widetilde{f}(k_x,k_y,z_o)]h(k_x,k_y,z_i - z_o) + n(k_x,k_y). \tag{6}$$

where n represents signal noise. Even in the absence of noise, the ability to reconstruct the object at z_o, given the image p at z_i, is limited by the cutoff spatial frequencies $k_x^2 + k_y^2 \leq \omega^2/c^2$, which serve as a low-pass filter. Following an

Clement, Huttunen, and Hynynen: Superresolution ultrasound imaging

argument outlined by Hunt,[8] it is noted that the convolution integral in Eq. (6) signifies the high-frequency components $(k_x^2 + k_y^2 > \omega^2/c^2)$ introduced by the object $\tilde{f}$ will affect the image $\tilde{p}(k_x, k_y, z_i)$ at spatial frequencies below the cutoff frequency. It is thus the task of the superresolution algorithm to infer the object shape, location, and intensity based on this partial amount of information.

It is assumed here that both the undisturbed beam $\tilde{p}(k_x, k_y, z_o)$ and the transfer function H are known for all k_x and k_y by *a priori* measurement of the field at z_o. As noted above, the ability to perform reconstruction with the information at the image plane is a result of the higher frequency information convolved into the signal. The success of reconstructing the object f is dependent on the ability to utilize this information. In the context of an inverse problem, the task becomes one of optimizing the likelihood of an estimated value for f over all k_x, k_y given $\tilde{p}(k_x, k_y, z_o)$ and a band limited $\tilde{p}(k_x, k_y, z_o)|_{k_x^2 + k_y^2 \leq \omega^2/c^2}$.

The reconstruction procedure starts by projecting the measured field from the image plane to the reconstruction plane, providing a band-limited representation of Eq. (6). The data are then analyzed using a simple optimization routine, which produces candidate values for the object function f as a function of object position, size, and intensity. The portion of each candidate image within $k_x^2 + k_y^2 \leq \omega^2/c^2$ is then compared to the actual projected image by calculating the sum of the difference between the two:

$$S(\alpha_1, \alpha_2, \ldots, \alpha_n)$$
$$= \sum_{k_x k_y} \left| \left(\tilde{p}_{\alpha_1, \alpha_2, \ldots, \alpha_n}(k_x, k_y, z_o) - \tilde{p}(k_x, k_y, z_o) \right) \big|_{k_x^2 + k_y^2 \leq \omega^2/c^2} \right|,$$

$$(7)$$

where S represents a single point on a multi-dimensional difference surface, and each dimension α_i represent a variable to be minimized (e.g., position of a single object, its intensity, and its location comprise three dimensions). The global minimum of this surface, if one exists, is selected as the reconstruction object f'.

Success of the algorithm centers on the ability to locate, at least to some desired precision, the position of this minimum on the mean difference surface. This requires particular attention to noise, as it relies on detecting subtle changes in the field. With this in mind, we examine below the effects of a simple numeric case with increasingly noisy data, paying particular attention to how it distorts the difference surface.

III. NUMERIC DATA

To initially demonstrate the approach under ideal conditions a simple two-dimensional simulation was set up, eliminating the y axis of Eq. (6), and seeking to resolve a 0.2-mm scattering object imbedded in a medium with properties similar to that of a homogeneous tissue ($c = 1560$ m/s) using a 1-MHz imaging beam. Two beams, one with a Gaussian-shaped amplitude profile (FWHM=2 mm) and the other with a step profile (width=4 mm), were separately considered, representing two significantly different spatial (angular) spectrums.

Simulations and data processing were implemented in Matlab 6.0 (Mathworks Inc, Natick, MA). The band-limited spectrum was calculated in the frequency domain by a discrete approximation to the Fourier integral,

$$\tilde{p}(k_x) = \frac{1}{\sqrt{2\pi}} \int p(x, z_o) f(x, z_o) e^{ikx} dx, \quad k_x < \omega/c, \quad (8)$$

simulating the measured signal at the object plane. This value was next compared with the known full spectrum of the beam profile, and the level of agreement between the two was determined. The two quantitative criteria for "agreement" used in the study are presented in Sec. V. Distortion was then added to the known beam profile corresponding to a guess in the object's size, location, and intensity, and the two signals were again compared. This was repeated in a loop for successively larger objects (increased at 0.04-mm increments) and with all possible positions using a spatial resolution of 0.04 mm.

The optimal reconstruction was first determined with the noise level set to zero. We then examined the effects of random white noise in the data and observed how it distorted the difference function. Complex broadband random noise of a controlled level was created with a pseudo-random number generator and added linearly to the measured field given by Eq. (6), causing both amplitude and phase distortion in the signal. Noise levels between 0% and 30% of the peak signal level were examined for the Gaussian signal. The field reconstruction was then performed and compared with the actual object size and location.

IV. LABORATORY MEASUREMENT

To demonstrate the algorithm in a controlled setting, we next attempted to image a series of successively thinner wires. The samples consisted of 0.6- and 0.3-mm nylon wires and finally a human hair (~ 0.03 mm). Success of the algorithm was determined by comparison of backprojection images with and without applying superresolution reconstruction. The apparent width of the wires was also measured from the reconstructed images and then compared with the actual wire diameter. We deliberately selected wires as the demonstration objects so that the reconstruction could be applied only along the y axis, similar to the numeric case. The algorithm was repeatedly applied along the direction perpendicular to the wire, so that the reconstruction of the two-dimensional image has superresolution applied only in one direction.

All measurements were made in a tank filled with degassed and deionized water. Inner walls of the tank were covered with rubber to prevent reflections. A multi-cycle sine waveform was generated by a 100-MHz synthesized arbitrary waveform generator (Wavetek, 395). The signal was sent to a rf power amplifier (ENI, A150) and then to a focused transducer. The waveform generator and the rf power amplifier remained the same during all of the measurements. Two different focused transducers were used: a single element transducer with driving frequency of 1.05 MHz
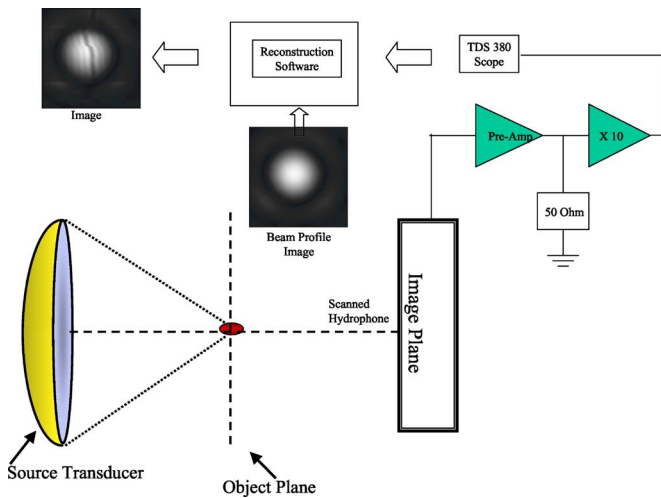
FIG. 1. (Color online) The experimental setup: A focused field is directed through the object plane and recorded at the image plane. This image is numerically back-projected to the object plane and reconstructed with a superresolution recovery method, using a stored beam profile image.
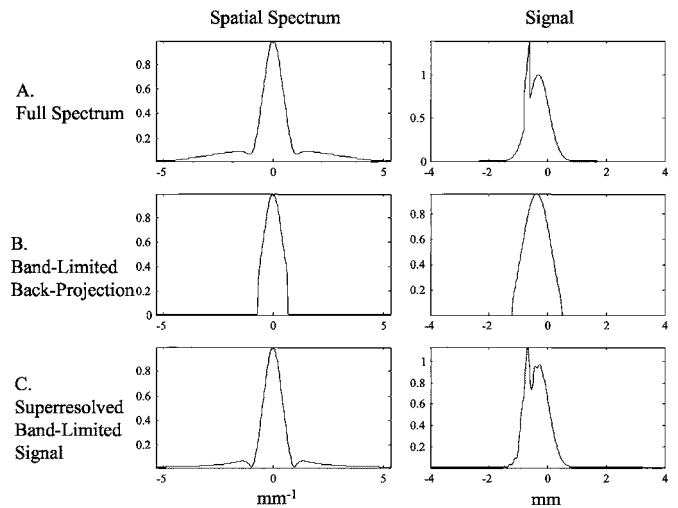

FIG. 2. A 2-mm object placed in a 1-MHz Gaussian-shaped beam. The true imaging signal and object (a) do not transmit sufficient spatial frequencies to reconstruct the object (b) unless superresolution recovery is used (c).

(diameter=25 mm radius=30 mm) and a 0.9 MHz driven at its fifth harmonic of 4.7 MHz (diameter=60 mm, radius =90 mm).

Signals were measured with a scanned hydrophone connected to a computer-controlled Parker 3D stepping motor-guided positioning system. An in-house manufactured 0.2 -mm hydrophone (ICBM01180102) was used for measurements at 1.05 MHz and a 0.075-mm polyvinylidene difluoride (PVDF) hydrophone (Precision Acoustics, SNS04) for measurements at 4.7 MHz. When using the PVDF hydrophone the signal was sent through a submersible preamplifier (Precision Acoustics, W210249). Both hydrophone signals were then amplified (Premeable Instruments, 1820 and LeCroy, DA1820A) before the time trace was recorded by a Tektronix (TDS 380, TDS 3012s) oscilloscope. A diagam of the setup is provided in Fig. 1.

Image reconstruction was implemented with a routine in Matlab. Before reconstruction, an autocorrelation function was applied between two images, one with and one without a wire. The autocorrelation was necessary to correct for slight motion of the field caused by thermally induced drifting or slight motions of the transducer. It is noted that this operation uses the same *a priori* field measurement that the superresolution method uses and does not require additional information. Object size was determined by measuring full width at half maximum (FWHM) from the backprojected image reconstruction.

V. RESULTS

A. Numeric study

The idealized (noiseless) simulated Gaussian-shaped field [Fig. 2(a)] was examined both with and without an object present, directly at the object plane. The image spectrum (left) and actual image (right) are both provided. For illustration, the object function is simulated as a net signal gain ("brightening" of the field), however the argument readily follows to cases where the object causes attenuation and/or

phase shift. Specifically, phase gain is described in the next section. Figure 2(b) shows the reconstructed image without superresolution compensation, when the acoustic image plane is located more than a few wavelengths from the object. When the difference surface S was examined, a global minimum was found and selected as the object size and location. Figure 2(c) shows the data reconstructed using the superresolution algorithm. Partial reconstruction of the higher spatial components is evident in the spatial frequency plot (left). The object was next deconvolved from the source beam, resulting in the normalized object identifications shown in Fig. 3. It is clear that without superresolution, the object, shown in Fig. 3(b), simply produces an artifact, which is indiscernibly related to the actual object. However, the algorithm reconstruction, in Fig. 3(c), produces improvement in both object localization and spatial dimensions. Similarly, Fig. 4(a) shows the stepped field directly after passing through the object plane. Figure 4(b) shows the re-
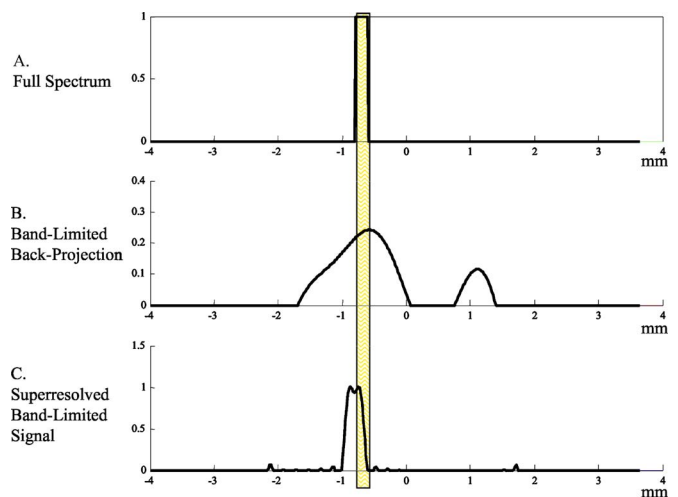

FIG. 3. (Color online) Simulation of a 2-mm object placed in a 1-MHz beam. The true imaging signal and object (a) do not transmit sufficient spatial frequencies to reconstruct the object (b) unless superresolution recovery is used (c).

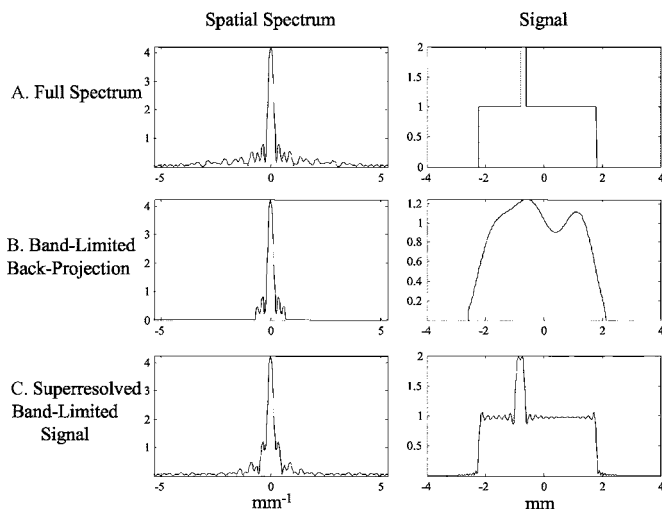Clement, Huttunen, and Hynynen: Superresolution ultrasound imaging

FIG. 4. Simulation of a 2-mm object placed in a 1-MHz step-shaped beam. The true imaging signal and object (a) do not transmit sufficient spatial frequencies to reconstruct the object (b) unless superresolution recovery is used (c).

constructed image without superresolution compensation, and Fig. 4(c) shows the same data reconstructed using the superresolution algorithm. As in the case with the Gaussian beam, the algorithm again successfully localized a stepped object, which contains a broadband spatial spectrum [Fig. 5(a)]. Figure 5(b) shows the reconstructed image without superresolution compensation, and Fig. 5(c) shows the same data using the superresolution algorithm.

The primary effect of noise on the difference surface was an overall gradient reduction or "flattening" of a region on the surface (Fig. 6), in many cases creating more than one global minimum. It is interesting to note that these reductions were both localized and centered around the minima present without noise suggesting that image recovery may be possible, even in the presence of a significant level of noise. In this preliminary study two possible recovery methods
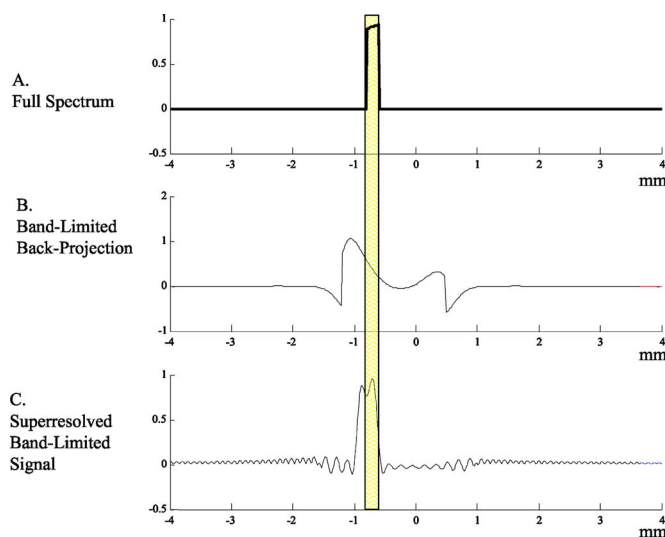

FIG. 5. (Color online) Simulation of a 2-mm object placed in a 1-MHz step-shaped beam. The true imaging signal and object (a) do not transmit sufficient spatial frequencies to reconstruct the object (b) unless superresolution recovery is used (c).
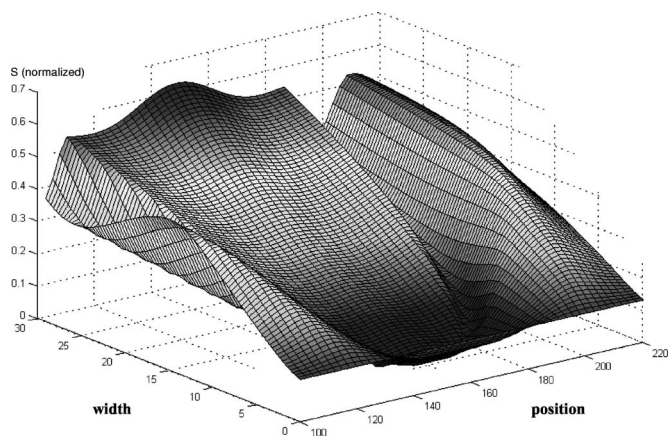

FIG. 6. Difference between the spectra produced by an image and candidate images containing different object positions and width. Introduction of a broadband noise was observed to flatten this surface about its global minimum.

were considered: The first method began by finding the 20 lowest values on the surface S. Next, the centermost position of these points was determined in a manner similar to a center-of-mass (COM) calculation:

$$\text{COM} = \frac{\sum_{n=1}^{N} S_n r_n}{\sum_{n=1}^{N} S_n}, \tag{9}$$

where S_n is the value of the difference function at surface position r. In the present case, r represents a two-dimensional vector with dimensions expressing object width and location, respectively. This central point on the surface provided the width and position of the object in the image. It is noted that the calculation given by Eq. (9) readily generalizes to higher dimensions.

The second method first determined the minimum along each position line of the surface (see Fig. 6). The mean minimum then determined the object position. Next, the minimum width at this position was identified. Results using both methods are shown as a function of noise in Fig. 7.

B. Laboratory-acquired images

To investigate the feasibility of applying the method to authentic ultrasound signals, a total of six samples were reconstructed—four samples were examined with 0.34-
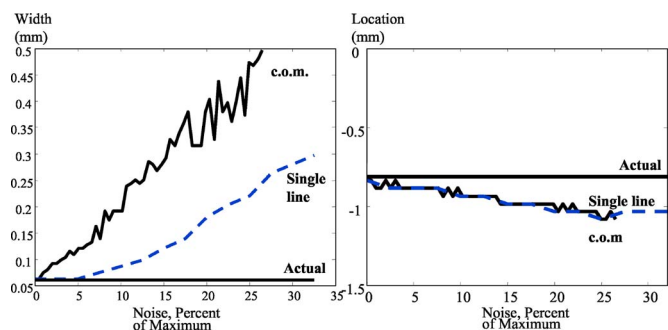

FIG. 7. (Color online) Graphs of actual width and location of an object compared with the predicted width and location as determined using two different techniques as a function of increasing noise.
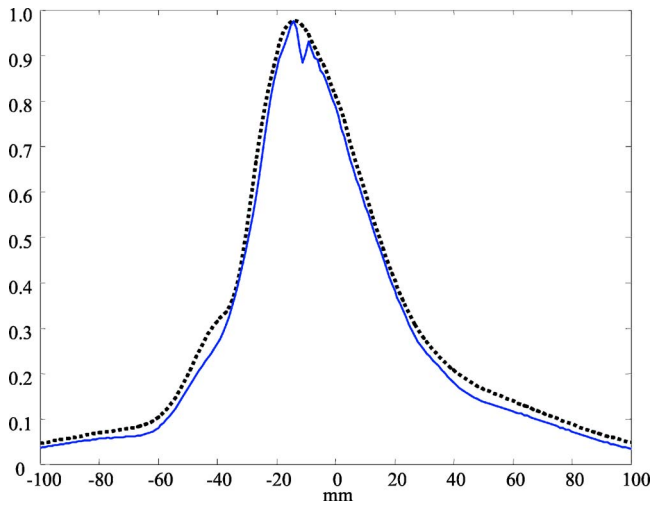
FIG. 8. (Color online) The on-axis backward-projected ultrasound signal before (dotted) and after (solid) a 0.34-mm nylon wire is placed in the focus of a 1.0-MHz field in water.

MHz nylon wire and a single sample each of 0.60-mm wire and 0.03-mm human hair. The 1.05-MHz transducer was used with the nylon wire and 4.70 MHz was used with the hair.

Initially, axial backprojections were performed to examine the evolution of the field along the axis of propagation. We discovered that these backprojections were highly sensitive to the presence of the wire, causing a reduction of image intensity near the object plane. As a result, we were able to use these images to identify the location of the object plane on the propagation axis. Figure 8 shows the on-axis projection before and after the 0.6-mm nylon wire was inserted. In this case there was a clearly visible reduction of the intensity at $z=-11$ mm. Using this information, high-resolution axial backprojections were performed in the x-z plane, perpendicular to the wire near $z=-11$, in order to identify the approximate location of the wire on the x axis, when compared to the same signal without a wire (Fig. 9, top). Similarly, high-resolution axial backprojections were performed in the y-z plane, perpendicular to the wire near the x-axis intersec-

TABLE I. Summary of measurements.

Frequency (MHz)	Wire thickness (mm)	Measured thickness (mm)	% difference
1.05	0.60	0.44	15
	0.34	0.29	7.9
		0.35	1.5
		0.35	1.5
		None detected	N/A
4.70	0.03	0.03	0

tion of the wire in order to identify the approximate location of the wire along the y-axis (Fig. 9, bottom).

Once the location of the image plane was identified, the image could be produced in the proper location. We back-projected the signal and constructed images both with and without the superresolution algorithm. This procedure was applied to the 0.60-mm wire, four cases with the 0.34-mm wire and one case with the 0.03-mm hair. The algorithm successfully identified the samples in five out of the six cases studied, the exception being one of the 0.34-mm measurements. The ability of the algorithm to identify the actual width of the object was considered after the reconstruction. A summary of the measurements is presented in Table I, showing that the wire (or hair) width was accurate to within an 15% difference in each of the cases where the sample was detected. However, in the case of the 0.60-mm wire, measurements were made on only 129 out of 220 image lines (59%), with failure to find the image in the remaining 91 lines. Comparison of images before [Fig. 10(a)1] and after a 0.34 mm wire was inserted [Fig. 10(a)2] indicated that the field experienced some distortion, but did not produce any sign of the wire. However, the same image with superresolution applied [Fig. 10(a)3] clearly shows an object through the focal area. Similarly, Figs. 10(b)1–3 illustrate the considerable image improvement experienced with superresolution applied to the human hair image.
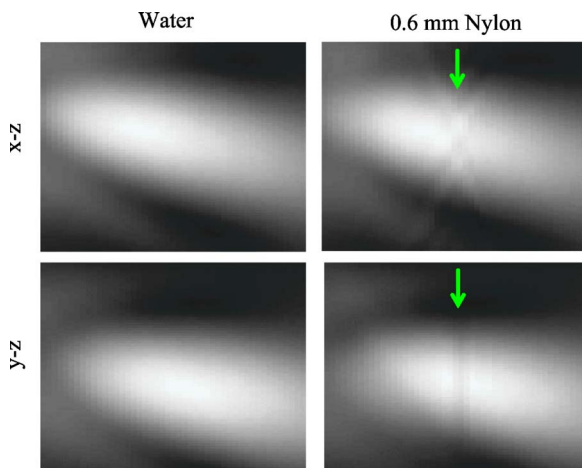

FIG. 9. (Color online) Axial back-projections of the signal before (left) and after (right) a 0.34-mm nylon wire is placed in the focus of a 1.0-MHz field in water.
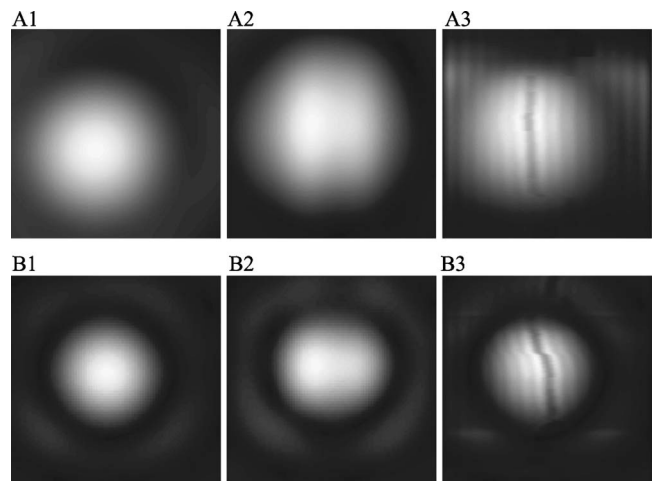

FIG. 10. Back-projected ultrasound field amplitude without 0.3 mm line (A1), with line (A2) and with line using superresolution. Series B shows the same but with a 0.03-mm human hair.

Clement, Huttunen, and Hynynen: Superresolution ultrasound imaging

VI. DISCUSSION

This investigation proposes an approach to enhanced ultrasound imaging and microscopy while providing an assessment of the ability of superresolved backprojected ultrasound to recover the location and dimensions of objects smaller than the imaging wavelength. The ability to detect objects at relatively low frequencies could ultimately allow imaging at greater penetration depths. The approach is related to procedures which have been described in optics, but with several key differences. First, in the present approach, ultrasound is backprojected from the image to the object plane. Second, most optical methods only consider the localization of the object and not the source beam itself, i.e., $p(x,y,z_o)$ in Eq. (5) is simply a step function. In contrast, ultrasound allows this beam to be modified by different transducer geometries. Third, by adjusting the ultrasound beam shape a series of different source functions $p(x,y,z_o)$ can be formed, providing additional spatial information.

Although the ability to perform the method in a controlled setting is by itself interesting, the method's feasibility becomes greatly enhanced by the observation that the method is stable in the presence of noise. It is interesting to note that the reconstruction accuracy was lower for the larger sized (0.6 mm) wire and more accurate with the objects much smaller than a wavelength, which is the region where superresolution is designed to be applied. Our relatively simple algorithm searched for objects in the size range from zero to the size of the ultrasound beamwidth.

Future work will concentrate on implementing higher-dimensional optimization routines in order to image complex structures within the beams. We will investigate the use of global terrain methods[33] to find surface extrema in the presence of noise.[34] Additionally, by passing multiple beams through the region with differing beamwidths, shape, and direction, a more complete image of the k-space region may be possible to improve the reconstruction.

With our simple experimental demonstration, we were able to detect a human hair with a diameter equal to approximately 0.09 wavelengths. This result introduces the use of the full complex wavefront information for reconstruction of image, which has not been used before in superresolution imaging. The use of ultrasound is expected to allow even more advanced methods to be used for the imaging, such as use of multiple ultrasound beam shapes (both amplitude and phase spatial distribution can be controlled) to bring out a broader range of spatial frequencies, which are later combined to reconstruct images in the object plane. The approach could potentially have application in detecting acoustic properties that are not visible with present diagnostic methods. In particular, the method would be sensitive to dynamic changes that induce a change in sound speed. Practical examples of such changes may include breast tumor imaging, internal temperature monitoring, and blood flow measurement, as well as many *in vivo* laboratory applications.

[1] D. Huang, E. A. Swanson, C. P. Lin, J. S. Shuman, W. G. Stinson, W. Chang, M. R. Hee, T. Flotte, K. Gregory, C. A. Puliafito, and J. G. Fujimoto, "Optical coherence tomography," Science **254**(1178), 1181 (1991).

[2] E. T. Ahrens, P. T. Narasimhan, T. Nakada, and R. E. Jacobs, "Small animal neuroimaging using magnetic resonance microscopy," Prog. Nucl. Magn. Reson. Spectrosc. **40**, 275–306 (2002).

[3] D. A. Knapik, B. Starkoski, C. J. Pavlin, and F. S. Foster, "A 100–200 MHz ultrasound biomicroscope," IEEE Trans. Ultrason. Ferroelectr. Freq. Control **47**, 1540–1549 (2000).

[4] F. S. Foster, C. J. Pavlin, and K. A. Harasiewicz, "Advances in ultrasound biomicroscopy," Ultrasound Med. Biol. **26**(1), 1–27 (2000).

[5] C. Passmann and H. Ermert, "A 100 MHz ultrasound imaging system form dermatologic and ophthalmologic diagnostics," IEEE Trans. Ultrason. Ferroelectr. Freq. Control **23**, 545–552 (1996).

[6] F. S. Foster, G. Liu, J. Mehi, B. S. Starkoski, L. Adamson, Y. Zhou, K. A. Harasiewicz, and L. Zan, "High frequency ultrasound imaging: from man to mouse," *IEEE 2000 Ultrasonics Symposium*, Vol. **2**, pp. 1633–1638.

[7] D. H. Turnbull, T. S. Bloomfield, H. S. Baldwin, F. S. Foster, and A. L. Joyner, "Ultrasound backscatter microscope analysis of early mouse embryonic brain development," Proc. Natl. Acad. Sci. U.S.A. **92**, 2239–2243 (1995).

[8] B. R. Hunt, "Super-resolution of imagery: Understanding the theoretical basis for the recovery of spatial frequencies beyond the diffraction limit," *Proceedings of Information Decision and Control 99* (Institute of Electrical and Electronic Engineers, Inc., New York, 1999).

[9] M. Ueda and T. Sato "Superresolution by holography," J. Opt. Soc. Am. **61**(3), 418–419 (1971).

[10] E. G. Williams, and J. D. Maynard, "Holographic imaging without the wavelength resolution limit," Phys. Rev. Lett. **45**(7), 554 (1980).

[11] M. A. Fink, "Time-reversed acoustics," Phys. Today **50**, 34–40 (1997).

[12] P. Blomgren, G. Papanicolaou, and H. Zhao, "Super-resolution in time-reversal acoustics," J. Acoust. Soc. Am. **111**, 230–248 (2002).

[13] W. Lukosz, "Optical systems with resolving powers exceeding the classical limit," J. Opt. Soc. Am. **56**(11), 1463 (1966).

[14] D. O. Walsh and P. A. Nielsendelaney, "Direct method for superresolution," J. Opt. Soc. Am. A Opt. Image Sci. Vis **11**(2), 572–579 (1994).

[15] N. Miura and N. Baba, "Superresolution for a nonnegative band-limited image," Opt. Lett. **21**(15), 1174–1176 (1996).

[16] A. Manikas, T. Ratnarajah, and J. S. Lee, "Evaluation of superresolution array techniques applied to coherent sources," Int. J. Electron. **82**(1), 77–105 (1997).

[17] M. Elad and A. Feuer, "Restoration of a single superresolution image from several blurred, noisy and undersampled measured images," IEEE Trans. Image Process. **6**(12), 1646–1658 (1997).

[18] K. B. Wolf, D. Mendlovoic, and Z. Zalevsky, "Generalized Wigner function for the analysis of superresolution systems," Appl. Opt. **37**(20), 4374–4379 (1998).

[19] I. Leiserson, S. G. Lipson, and V. Sarafis, "Superresolution in far-field imaging," Opt. Lett. **25**(4), 209–211 (2000).

[20] I. Leizerson, S. G. Lipson, and V. Sarafis, "Superresolution in far-field imaging," J. Opt. Soc. Am. A Opt. Image Sci. Vis **19**(3), 436–443 (2002).

[21] W. X. Sheng and D. G. Fang, "Angular superresolution for phased antenna array by phase weighting," IEEE Trans. Aerosp. Electron. Syst. **37**(4), 1450–1458 (2001).

[22] E. A. Ash and G. Nicholls, "Super-resolution aperture scanning microscope," Nature (London) **237**(5357), 207 (1972).

[23] T. R. M. Sales and G. M. Morris, "Fundamental limits of optical superresolution," Opt. Lett. **22**(9), 582–584 (1997).

[24] S. Wadaka and T. Sato, "Superresolution in incoherent imaging system," J. Opt. Soc. Am. **65**(3), 354–355 (1975).

[25] M. Ueda and T. Sato, "Superresolution by holography," J. Opt. Soc. Am. **61**(3), 418 (1971).

[26] F. Boada, E. M. Haacke, W. Tobocman, K. Santosh, and Z.-P. Liang, "Superresolution imaging applied to ultrasonic scattering," Inverse Probl. **5**, L21–L25 (1989).

[27] A. D. Pierce, *Acoustics, An Introduction to its Physical Principles and Applications* (Acoustical Society of America, Woodbury, NY, 1989).

[28] P. R. Stepanishen and K. C. Benjamin, "Forward and backward projection of acoustic fields using FFT methods," J. Acoust. Soc. Am. **71**, 803–812 (1982).

[29]G. T. Clement and K. Hynynen, "Field characterization of therapeutic ultrasound phased arrays through forward and backward planar projection," J. Acoust. Soc. Am. **108**(1), 441–446 (2000).

[30]M. Kaveh, M. Soumekh, and J. F. Greenleaf, "Signal processing for diffraction tomography," IEEE Trans. Sonics Ultrason. **SU-31**(4), 230–239 (1984).

[31]G. T. Clement and K. Hynynen, "Forward planar projection through layered media," IEEE Trans. Ultrason. Ferroelectr. Freq. Control **50**, 1689– 1698 (2003).

[32]G. T. Clement, P. J. White, and K. Hynynen, "Enhanced ultrasound transmission through the human skull using shear mode conversion," J. Acoust. Soc. Am. **115**, 1356–1364 (2004).

[33]A. Lucia and Y. Feng, "Global terrain methods," Comput. Chem. Eng. **26**, 529–546 (2002).

[34]H.-F. Cheng, "Optimization based on information containing uncertainties," Kybernetes **30**(9), 1177–1182 (2001).

Clement, Huttunen, and Hynynen: Superresolution ultrasound imaging